applied optics

Finding point method and re-optimized method for the brightness temperature simulation from Fengyun 4A AGRI in infrared channels

MINGWEI ZHU,[1] SHUANGGEN JIN,[1,2,3,*] AND DI DI[4,5]

[1]*School of Remote Sensing and Geomatics Engineering, Nanjing University of Information Science and Technology, Nanjing 210044, China*
[2]*Shanghai Astronomical Observatory, Chinese Academy of Sciences, Shanghai 200030, China*
[3]*School of Surveying and Land Information Engineering, Henan Polytechnic University, Jiaozuo 454000, China*
[4]*Collaborative Innovation Center on Forecast and Evaluation of Meteorological Disasters, Nanjing University of Information Science and Technology, Nanjing 210044, China*
[5]*Key Laboratory for Aerosol-Cloud-Precipitation, China Meteorological Administration, School of Atmospheric Physics, Nanjing University of Information Science and Technology, Nanjing 210044, China*
*Corresponding author: sgjin@shao.ac.cn

The correlated *k*-distribution (CKD) is a fast radiative transfer model and is often used in atmospheric absorption simulation. In the paper, we apply two automatic CKD methods to satellite brightness temperature simulations from the Fengyun 4A Advanced Geostationary Radiation Imager (AGRI) in infrared channels, namely, the finding point method (FPM) and the re-optimized method (ROM). In the calculation, we used Radiative Transfer for the Television Observation Satellite Operational Vertical Sounder (RTTOV) as the comparison, and we use line-by-line (LBL) integration as the reference. Compared with LBL in the brightness temperature simulation of real profiles, the errors of FPM in 7.1 μm and 13.5 μm channels are 0.22 K, −0.13 K for mean error and 0.3128 K, 0.2184 K for root mean square error (RMSE), respectively, which are larger than that of RTTOV, with 0.16 K, 0.02 K, 0.2144 K, and 0.1226 K, respectively. In the other channels, the results show that of ROM has the highest accuracy and RTTOV has the lowest accuracy. In general, FPM and ROM can achieve very good accuracy in satellite infrared remote sensing. © 2022 Optica Publishing Group

https://doi.org/10.1364/AO.472382

1. INTRODUCTION

Nomenclature

AGRI	Advanced geostationary radiation imager
CKD	Correlated-*k* distribution method
DM	Decreasing method
FPM	Finding point method
LBL	Line-by-line method
LBLRTM	Line-by-Line Radiative Transfer Model
ME	Mean error
MT_CKD	Water vapor continuum model
ROM	Re-optimized method
RTTOV	Radiative Transfer for the Television Observation Satellite Operational Vertical Sounder
RMSE	Root mean square error
SRF	Spectral response function
TOA	Top of atmosphere
$c_{x_i,\ P_j^r, i}$	The *i*th fitting coefficient for temperature in x_i integration point and *j*th reference pressure

(Table continued)

$f(k)$	Probability density
g	Cumulative probability function
Δg_i	Weight point for *i*th CKD integration point
k	Absorption coefficient
k^r	Absorption coefficient in reference pressure
$k_{\max}$	Maximum absorption coefficient in reference level
$p(i_1, i_2)$	Combination point consisted of x_{i_1} of gas 1 and x_{i_2} of gas 2
n	Total number of CKD integration points
$p(i_1, i_2)$	Combination point consisted of x_{i_1} of gas 1 and x_{i_2} of gas 2
P	Atmospheric pressure
P_j^r	*j*th reference pressure
r	Ratio of heating rate error function
T	Atmospheric temperature
Tr	Transmission
v	Wavenumber
Δv	Spectral interval
x_i	Position point for *i*th CKD integration point

The broadband satellite infrared sounding instrument observation can be used in the cloud detection and clearing scheme, which is important in atmospheric science study. As

an important part of the cloud retrieval algorithm, the calculation of atmospheric radiation absorption must be very fast and accurate because the model will be called many times during the iterations [1–5]. Among the transfer models, the line-by-line (LBL) method is the most accurate method. However, the LBL method needs to perform the numerical integration of the Voigt broadening for all spectral lines. Therefore, its calculation amount and speed cannot satisfy the application. Compared with practical applications, LBL is more suitable as a reference for fast radiation calculation schemes. Fast calculation schemes are a parametric alternative to LBL because they are fairly fast and have relatively satisfactory accuracy. The correlated *k*-distribution (CKD) method is a commonly used fast calculation scheme. CKD assumes the gaseous absorption coefficients in wavenumber space vary with the same trend in all atmosphere levels. Thus, the absorption coefficients in different atmospheric layers can be monotonously sorted according to the intensity. Then CKD can use much fewer points to calculate the gaseous transmissivity than the LBL. In other words, CKD can get comparable accuracy with LBL with much faster speed [6–10]. Furthermore, CKD can solve the gaseous multiple scattering and overlapping absorption in the inhomogeneous atmosphere with aerosols and clouds for its simple and practical property, so it has been applied to broadband satellite infrared sounding in recent decades [11–15].

While CKD has such advantages, it becomes difficult when applied in the overlapping spectral bands. The overlapping problem happens in most cases. Furthermore, the method treated for overlapping problems can affect the accuracy and efficiency of radiative transfer calculations in the CKD. Thus, how to deal with the overlapping bands with good performance has become the key problem of CKD [7,16–19]. In the past decades, several studies proposed their methods to solve the overlapping problem based on CKD. The first approach is the correlated spectra scheme. It assumes that the absorption coefficient distribution trends of all gases are perfectly correlated with each other. Obviously, the assumption does not meet the actual situation.

The second approach is the uncorrelated spectra scheme, in which the total transmittance of a mixed gas is equal to the transmittance products from all gases. However, the property can only be applied to the monochromatic transmittance. For a limited interval like satellite observation channel, this method is applicable if and only if the transmittance of the two gases is completely uncorrelated, i.e., the distribution of their absorption coefficients in the spectral interval is completely random. Therefore, this scheme is not applicable for practical situations due to the non-random-induced correlation [17]. Besides, the radiation transmittance programs need to be called in many times for the scattered atmosphere due to the multiple summation. Assuming the number of absorption gases in a spectral band is n_{mol}, the number of integration points for each gas is n. Then, transmittance programs need to be called for $N = n^{n_{mol}}$ times. When an additional gas with an integral number of L is added, the calculation amount will increase by L times. Therefore, the calculation speed is not satisfactory.

The last method is a partly correlated scheme, for example, the alternate mapping CKD method and modified amount weighted scheme. In alternate mapping CKD, the cumulative probability space is divided into several subintervals. Then, we

pick a "reference gas" and sort its absorption coefficients, while the other gases are sorted in the same sorting rule. We take the average absorption coefficient of the first subinterval and multiply it by the adjust factor. Next, we choose another "reference gas" and repeat the operation for the second and subsequent subintervals. However, this method requires manual operation, and the accuracy is limited. For example, alternate mapping CKD requires researchers to manually divide the subinterval in bands, choose the "reference gas" that dominates the absorption in each subinterval, and estimate the adjustment factors of the gas absorption coefficients in each subinterval. Therefore, it consumes a lot of labor and introduces manual error in building the algorithm [16,17]. For the modified amount weighted scheme, the main idea is appropriately combining the absorption coefficients of participating gases into a "single gas." While the modified amount weighted scheme has achieved high accuracy as it can bypass the problem of gaseous overlapping, the handling of weighting factors for each gas becomes inefficient when the overlapping band contains over two gases [9,16].

Above all the methods, Nakajima proposed the decreasing method (DM) [19], which is an automatic method based on traditional CKD theory. The DM can avoid the error introduced by the manual operation. However, the accuracy of this method still can be improved. Recently, this method has been improved to the finding point method (FPM) and re-optimized method (ROM) [18]. Compared with the other CKD method, FPM and ROM can achieve high accuracy and avoid manual errors. DM has been successfully applied in remote sensing models and achieved satisfactory results, but the more accurate FPM and ROM have not been used. In this paper, we applied these two methods to satellite remote sensing calculation, and we improve the accuracy of brightness temperature simulation. In Section 2, the brief description of the CKD method and the modifications of FPM and ROM are introduced. Section 3 introduces the simulation results of FPM and ROM, and compares them with the results calculated by Radiative Transfer for the Television Observation Satellite Operational Vertical Sounder (RTTOV). Section 4 provides concluding remarks.

2. PARAMETERS OF AGRI

The Advanced Geostationary Radiation Imager (AGRI) on Fengyun 4A is mainly responsible for the task of acquiring cloud images, including 14 channels, which is nearly 3 times the 5 channels of Fengyun-2. The information of AGRI is shown in Table 1. Among them, there are six short-wave channels, including two visible light channels. The observed energy comes from the sun, which is mainly used to detect the information of solar energy reflected by the surface or atmosphere during the daytime. Channels 7 and 8 are medium-wave infrared channels. Since the medium-wave infrared channel can detect information from the sun as well as information from the surface and clouds, the radiant energy varies greatly. AGRI channels 7 and 8 are used to detect high temperature and low temperature, respectively. The setting can effectively take into account the need to detect high temperature and low temperature targets at the same time. Channels 9 to 14 are long-wave infrared channels, including two water vapor channels, one carbon dioxide channel, and three atmospheric window channels. The water vapor channels can reflect the water vapor information in the

Table 1.   Fengyun 4A AGRI Information

Channel	Type	Central Wavelength	Spatial Resolution	Main Purpose
1	Visible and	0.47 μm	1 km	Aerosol
2	near-infrared	0.65 μm	0.5–1 km	Fog, cloud
3		0.825 μm	1 km	Vegetation
4	Short-wave	1.375 μm	2 km	Cirrus
5	Infrared	1.61 μm	2 km	Cloud, snow
6		2.25 μm	2–4 km	Cirrus, aerosol
7	Mid-wave	3.75 μm	2 km	Fire
8	infrared	3.75 μm	4 km	Land surface
9	Water vapor	6.25 μm	4 km	High level water vapor
10		7.1 μm	4 km	Middle level water vapor
11	Long-wave	8.5 μm	4 km	Water vapor, cloud
12	infrared	10.7 μm	4 km	Surface temperature
13		12.0 μm	4 km	Surface temperature
14		13.5 μm	4 km	Cloud thickness

middle and upper layers of the troposphere, and channel 14 is the carbon dioxide absorption band.

In addition to the detection content of clouds, water vapor, vegetation, and ground surface observed by Fengyun-2, it also has the ability to capture aerosols and snow, and it can clearly distinguish different phases of clouds and high- and mid-layer water vapor. Compared with the limitation of a single visible light channel of Fengyun-2, Fengyun-4 produced a color satellite cloud image for the first time and generated regional observation images at the fastest 1 min.

Spectral response function (SRF) refers to the ratio of the received radiance to the incident radiance of the sensor at each wavelength (Fig. 1). Due to sensor hardware limitations, the response of the sensor within a predetermined wavelength range cannot be 100%. Otazu *et al.* pointed out that the SRF of a sensor defines the probability that the sensor detects photons of a given frequency and mathematically deduces and analyzes the proportional relationship between the response of panchromatic and multispectral sensors to radiant energy from the perspective of probability [20].
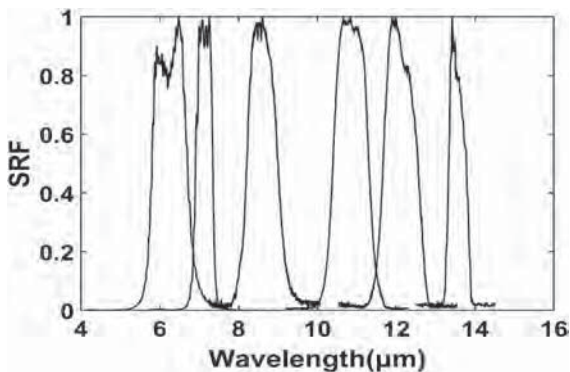
Fig. 1.   Spectral response functions of AGRI 9-14 channels.

3. THEORY AND METHODS

In LBL, the radiance of the atmosphere in the calculation varies with the wavenumber. Therefore, the transmittance function for a single gas has to be written as [7]

$$\text{Tr}_{\text{LBL}} = \frac{\int_{\Delta v} I(v) e^{-k(v)u} \mathrm{d}v}{\int_{\Delta v} I(v) \mathrm{d}v}, \tag{1}$$

where we use Tr_{LBL} to denote the transmittance; I is the monochromatic radiance spectrum, which is a function of the wavenumber; v is wavenumber, and Δv is the spectral interval; k is the absorption coefficient; and u is the absorber amount. The average transmittance function of CKD can be written as

$$\text{Tr}_{\text{CKD}} = \frac{1}{\Delta v} \int_{\Delta v} e^{-k(v)u} \mathrm{d}v$$

$$= \int_0^\infty f(k) e^{-ku} \mathrm{d}k$$

$$= \int_0^1 e^{-k(g)u} \mathrm{d}g$$

$$= \sum_{i=1}^N e^{-k(x_i)u} \Delta g_i, \tag{2}$$

where Tr_{CKD} is the transmittance of CKD; $f(k)$ is the probability distribution function for the gaseous absorption coefficient, which is defined as $f(k) = \frac{1}{\Delta v}|\frac{dv}{dk}|$; n is the total number of integration points; $k(x_i)$ is the absorption coefficient in x_i; u is the absorber amount; g is the cumulative probability function, which is defined as $g(k) = \int_0^k f(k)\mathrm{d}k$; and x_i and Δg_i denote integration point and weight, respectively, for ith point. CKD uses the integral value of atmospheric blackbody radiation in the calculated [21,22], while the radiance of the atmosphere in the calculation of LBL varies with the wavenumber. However, the blackbody radiation does not vary much with the wavenumber. Therefore, we can adjust the weights Δg_i in CKD to cover the influence of the variation of blackbody radiation in LBL, i.e., make adjusted $\text{Tr}_{\text{CKD}} = \sum_{i=1}^N e^{-k(x_i)u} \Delta g_i$ and Tr_{LBL} equal.

SRF of the measurement instrument has a great influence on the results. Therefore, we need to include the influences of the SRF. The average transmittance function has been rewritten as [5]

$$\text{Tr}'_{\text{LBL}} = \frac{\int_{\Delta v} I(v)\varphi(v) e^{-k(v)u} \mathrm{d}v}{\int_{\Delta v} I(v)\varphi(v) \mathrm{d}v}, \tag{3}$$

where φ is SRF. Including the SRF in CKD, Eq. (2) is rewritten as

$$\text{Tr}_{\text{CKD}} = \frac{1}{\Phi} \int_{\Delta v} \varphi(v) e^{-k(v)u} \mathrm{d}v = \int_0^\infty f'(k) e^{-ku} \mathrm{d}k$$

$$= \int_0^1 e^{-k(g')u} \mathrm{d}g' = \sum_{i=1}^N e^{-k(x_i)u} \Delta g'_i = \text{Tr}'_{\text{LBL}}, \tag{4}$$

where $\Phi = \int_{\Delta v} \varphi(v)\mathrm{d}v$, and the probability distribution function is rewritten as
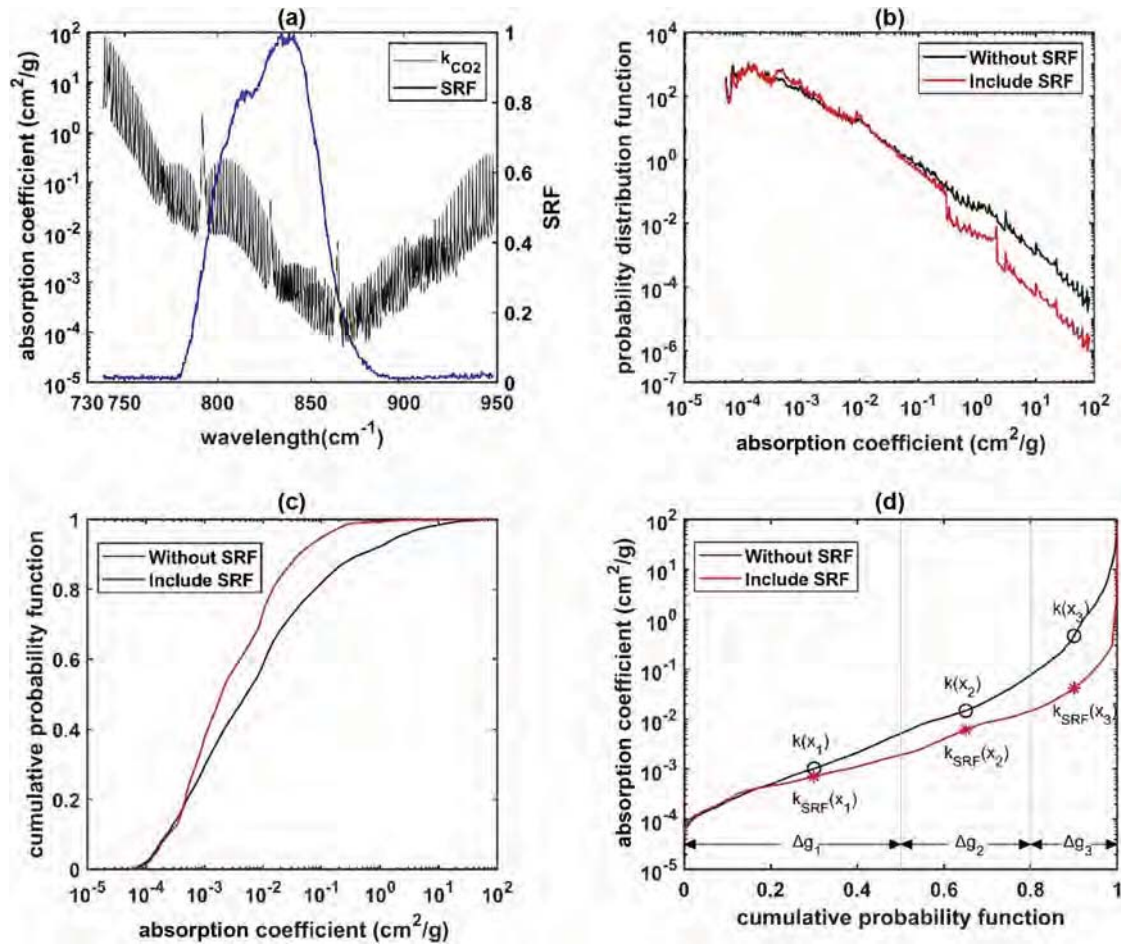
Fig. 2. (a) Absorption coefficient as a function of wavenumber and spectral response function. (b) Probability distribution as a function of absorption coefficient. (c) Cumulative probability as a function of absorption coefficient. (d) Absorption coefficient as a function of cumulative probability. In (b)–(d), the red lines included the spectral response function, and the black lines are without the inclusion of the spectral response function.

$$f'^{(k)} = \frac{1}{\Phi} \left| \frac{dv \cdot \varphi(v)}{dk} \right|. \tag{5}$$

Figure 2 shows a sample of the transformation relationship between the probability distribution function and the cumulative probability function, and the difference between the result without SRF and the result including SRF. Figure 2(d) shows the meaning of x_i, $k(x_i)$ and Δg_i. $k(x_i)$ is the absorption coefficient $k(g)$ at x_i of the cumulative probability function, and Δg_i is the corresponding weight of $k(x_i)$.

In the FPM, we parameterized absorption coefficient k as a function of temperature polynomial for each reference pressures. The polynomial is shown as follows:

$$k^r(x_i, P_j^r, T) = \sum_{t=1}^{5} c_{x_i, P_j^r, t} \cdot (T - 250)^{t-1}, \tag{6}$$

where P_j^r represents the jth reference pressure, and $c_{x_i, P_j^r, i}$ denotes the fitting coefficient of the temperature in each reference pressure and integration point. Totally 21 reference pressure levels are distributed between 1000 and 0.1 mb. For temperatures between 160 and 340 K, Eq. (6) is valid, including the most atmospheric conditions [16]. The absorption

coefficient $k(x_i, P, T)$ is approximated by the linear interpolation between two neighboring P_j and P_{j+1}. However, as we included SRF in calculation, the absorption coefficient in each integration point of cumulative probability space varies significantly. Then, the approximation in Eq. (6) can lead to negative values, which does not meet the definition of the absorption coefficient (e.g., the water self-continuum absorption coefficient in 7.1 μm channel shown in Fig. 3). Therefore, we changed the temperature fitting polynomial as

$$k^r(x_i, P_j^r, T) = \exp\left(\sum_{t=1}^{5} c'_{x_i, P_j^r, t} \cdot (T - 250)^{t-1}\right). \tag{7}$$

Figure 3 shows two temperature fitting polynomials of the water self-continuum absorption coefficient in 7.1 μm channel, and the yellow dots are fitting sampling points. The modified polynomial better agrees with the physical properties of the absorption coefficient than the original polynomial Eq. (6).

An essential problem of the CKD method is overlapping absorption. The FPM is an improved method of the traditional CKD [18], which nonlinearly optimizes the overlapping problem and gets more accurate combination of quadrature points with weights simultaneously. The radiative flux and
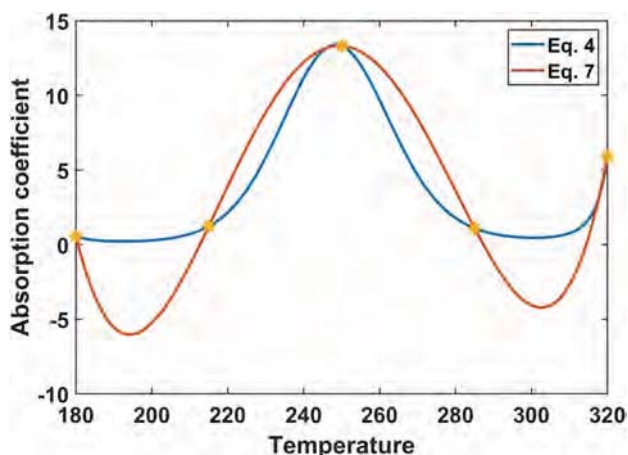
Fig. 3. Comparison of two temperature fitting polynomial of water self-continuum absorption coefficient in the third point of 7.1 μm channel. The yellow dots are fitting sampling points of LBL.

heating rate profiles from LBL and CKD at each quadrature point are regarded as highly dimensional vectors. That is, those vectors at each CKD point need to be linearly combined into the vector of LBL. In other words, we transformed the original overlapping problem into a simpler nonlinear programming problem. Furthermore, FPM assumes the cumulative probability functions of each gas are perfectly uncorrelated [as shown in Fig. 4(a)], and the Gaussian integration point is taken as the sampling point of the absorption coefficient for all gases. The number of absorption gases is n_{mol} in a spectral band (typically, there are no more than three kinds of gases in each band), the number of Gaussian integration points is n, and then the number of quadrature points is $N = n^{n_{mol}}$. The function of FPM is to select the optimal combination from N quadrature points as the CKD solution. The transmittance function of each quadrature point is shown as follows:

$$\text{Tr}(x_{i1}, x_{i2}, x_{i3}) = e^{-(k_1(x_{i1})u_1 + k_2(x_{i2})u_2 + k_3(x_{i3})u_3)}, \quad \textbf{(8)}$$

where x_{i1}, x_{i2}, x_{i3} are, respectively, the $i1$th, $i2$th, $i3$th integration points for gas1, gas2, gas3; $k_1(x_{i1}), k_2(x_{i2}), k_1(x_{i3})$ are, respectively, the absorption coefficient of gas1, gas2, gas3 in

x_{i1}, x_{i2}, x_{i3}. u_1, u_2, u_3 are, respectively, the absorber amount of gas1, gas2, gas3.

To get the m th-order result, FPM selects a point from the N quadrature points so that its combination with the $(m-1)$th order result can minimize the objective function. Then, FPM replaces each point with its neighboring point, recalculates weights and the objective function of each combination with neighboring point, and saves the neighboring point with the smallest objective function. This step is repeated until the objective function is minimum. The operations are repeated for all orders. The details of FPM are shown in the works of Zhu *et al.* [18]. Taking an example of two gases, the integration point x_{i1} of gas 1 and the integration x_{i2} of gas 2 are combined to form the quadrature point $p(i_1, i_2)$. In FPM, the neighboring point of $p(i_1, i_2)$ is $p(i_1 \pm 1, i_2 \pm 1)$. We modified the neighboring point as $p(j_1, j_2)$, $i_1 - R \leq j_1 \leq i_1 + R$, $j_1 \in Z$, $i_2 - R \leq j_2 \leq i_2 + R$, $j_2 \in Z$, where R is the radius of each integration point's neighbor area. For example, $p(3, 3)$ shown in Fig. 4(b) with R is set as 2, and the points covered in the red area are all its modified neighboring points.

We tried three different radii when FPM replaces each point with its neighboring point. The larger the value of the radius we set, the greater amount of calculation we have. Therefore, we only calculated the results under three values of the radius. Specifically, when the radius is set as 1, the modified points are the same as original definition in FPM. Table 2 shows the objective functions of 7.1 and 12 μm channels under three values of the radius. When the number of integration points is 1, FPM can directly select the optimal solution when screening all points. Therefore, the objective function values under all radiuses are the same. As the number of integration points increases, the objective functions under different radiuses decrease, and the smallest objective function appears under a different radius. For example, in 7.1 μm channel, when the number of integration points is 4, the objective functions under the radius of 1 and 3 are the smallest; when the number of integration points is 6, the objective function under the radius of 2 is the smallest, while the objective function under the radius of 1 is the largest. A similar phenomenon can be observed in 12 μm and the other channels. In conclusion, we can choose the result under a different value of radius to obtain the best results according to the different requirements of the calculation
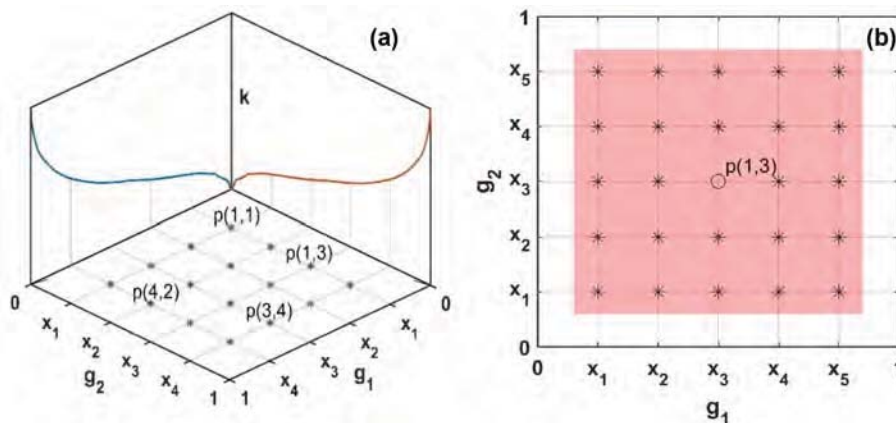
Fig. 4. (a) Example of perfectly uncorrelated treatment of two gases. (b) Example of the modified neighboring point. The point is $p(3, 3)$; the radius R is set as 2.

Table 2.   Comparison of Objective Function of FPM under Three Different Radiuses

	Radius					
	7.1 µm			12 µm		
NP[a]	1	2	3	1	2	3
1	97.5256	97.5256	97.5256	154.7020	154.7020	154.7020
2	79.4161	79.4161	79.4161	17.6616	34.4463	17.6616
3	7.2099	11.6883	7.2099	6.4087	14.5144	6.4087
4	4.4004	7.3327	4.4004	4.5836	10.0388	4.5836
5	3.1598	4.1100	2.9634	2.1061	2.0127	2.2027
6	2.7341	1.2368	2.4509	1.6124	1.5355	1.6002

[a]NP, number of integration points.

speed. When the radius is larger than the number of Gaussian integration points, the result of FPM is the global optimal solution. However, when there is more than one absorber in the channel or the number of integration points is too large, the computational complexity of FPM is too large and even exceeds the calculation capacity of the computer. Therefore, we set the radius not to exceed 3.

The accuracy of FPM is satisfied but limited by the number of Gaussian quadrature points. Therefore, the ROM used the adjusted factors to minimize the objective function, which are shown below:

$$\begin{cases} \alpha_{r,i} * k_r(x_i, P_j^r, T) > 0 \\ \alpha_{r,i} * k_r(x_i, P_j^r, T) - k_{\max}(P_j^r, T) \leq 0 \end{cases}, \quad \text{(9)}$$

where $\alpha_{r,i}$ denotes the adjusted factor for ith absorption coefficient fitting polynomial and $k_{\max}$ denotes the maximum absorption coefficient in each reference level, which is also expressed as a function of temperature polynomial: $k_{\max}(P_j^r, T) = \exp\left(\sum_{t=1}^{5} c'^{\max}_{P_j^r,t} * (T - 250)^{t-1}\right)$, where $c^{\max}_{P_j^r,t}$ is the fitting coefficient for temperature in each reference pressure. Since the number of integration points in remote sensing simulation is small, we can use more adjusted factors to make

ROM more accurate, and we have changed temperature polynomial to ensure the absorption coefficients are larger than 0; thus, the first constraint in Eq. (9) becomes inactive. Equation (9) becomes

$$\alpha_{r,i} * k_r(x_i, P_j^r, T) - k_{\max}(P_j^r, T) \leq 0. \quad \text{(10)}$$

4. RESULTS AND ANALYSIS

A. Standard Profiles

In this study, we used the Line-By-Line Radiative Transfer Model (LBLRTM v12.8), Water Vapor Continuum Model (MT_CKD v3.1), and RTTOV (v13.0) in our calculation, and we used the High Resolution Transmittance spectral database (HITRAN2016; https://hitran.org) and 83 standard profiles (https://nwp-saf.eumetsat.int/downloads/profiles/ECMWF_8 3P_91L.dat) as the input data. Figure 5 shows the brightness temperature errors of FPM, ROM, and RTTOV at different zenith angles for all infrared channel under standard profiles; the blue lines, yellow lines, and red lines are the errors of RTTOV, FPM, and ROM; the solid lines and dashed lines are root mean square errors (RMSEs) and mean errors (MEs). In 7.1 µm channel, the ME of RTTOV is similar to that of ROM, while the RMSE of RTTOV is larger than that of ROM. In contrast, FPM has the largest error in the 7.1 µm channel. In the 8.5 µm channel, RTTOV has the lowest accuracy. The ME and RMSE of ROM are all larger than FPM. In this case, we can choose FPM with better accuracy instead of ROM in the subsequent calculation. Although the accuracy of ROM is slightly lower than that of FPM, the accuracy of ROM is not lower than RTTOV. In the other channels, ROM has the highest accuracy, while RRTOV has the lowest accuracy. Table 3 illustrates the ME and RMSE of the three algorithms under all zenith angles. The result is similar to that of Fig. 5: the errors of FPM are less than those of RTTOV except for the 7.10 µm channel, and ROM is more accurate than RTTOV in all results.
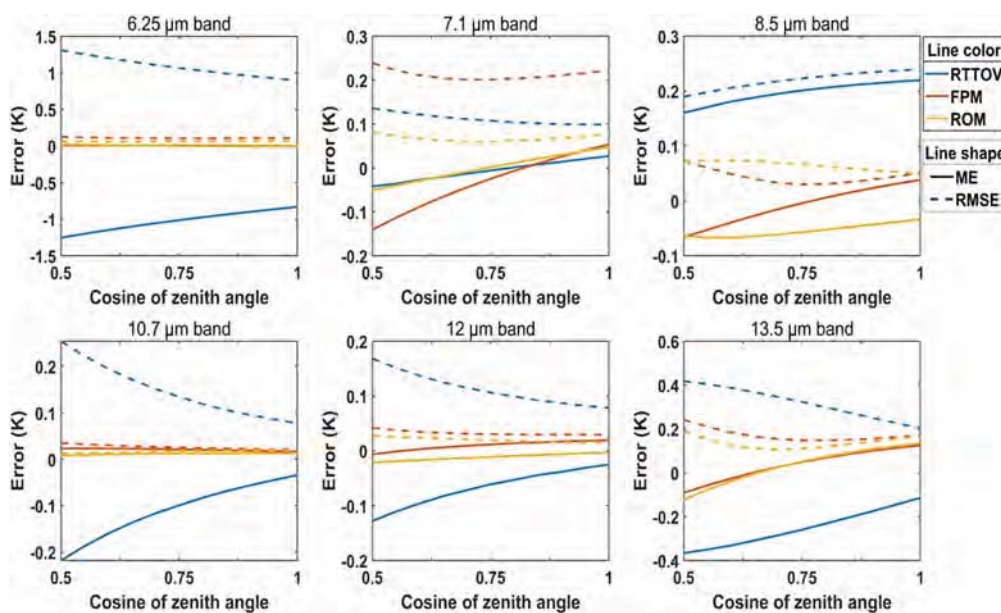
Fig. 5.   ME and RMSE of RTTOV, FPM, and ROM vary with the cosine of the zenith angle.

Table 3. Comparison of ME and RMSE of FPM, ROM, and RTTOV under 83 Standard Profiles

Channel	Me (K)			RMSE (K)		
	RTTOV	FPM	ROM	RTTOV	FPM	ROM
6.25 μm	−1.0245	0.0032	0.0027	1.0879	0.1103	0.0641
7.10 μm	−0.0066	−0.0320	0.0004	0.1120	0.2128	0.0682
8.50 μm	0.1968	−0.0081	−0.0541	0.2204	0.0459	0.0650
10.8 μm	−0.1095	0.0205	0.0115	0.1567	0.0266	0.0168
12.0 μm	−0.0673	0.0098	−0.0114	0.1164	0.0328	0.0206
13.5 μm	−0.2514	0.0362	0.0334	0.3256	0.1742	0.1398
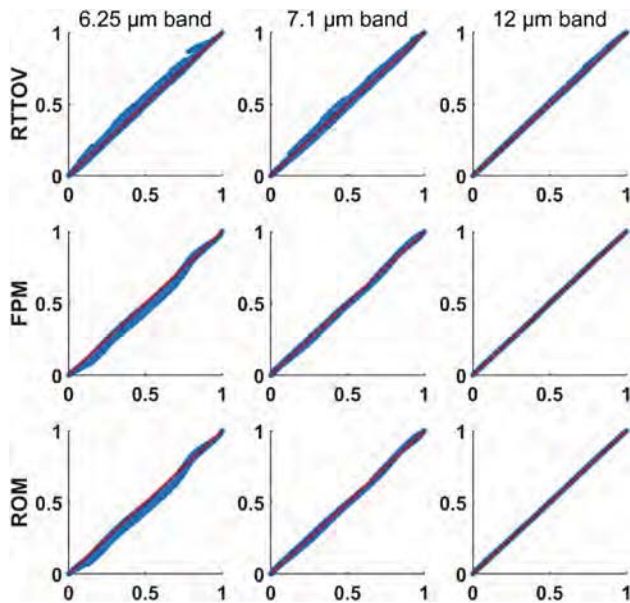
Fig. 6. Comparison of the transmittance from level to TOA calculated by RTTOV, FPM, ROM, and LBL under clear sky in 83 standard profiles.

We only calculated the brightness temperature under a clear sky to avoid the influence of the cloud parameterization because the influence of cloud is greater than atmosphere in the calculation. In the calculation, transmittance is a better indicator of computational accuracy. Therefore, we calculated the average transmittance from level to the top of atmosphere (TOA) of three methods and compared them with LBL.

Figure 6 shows the comparison of the transmittance from level to TOA calculated by RTTOV, FPM, ROM, and LBL under clear sky in 83 standard profiles for 6.25, 7.1, and 12 μm channel. The errors of FPM are almost the same as ROM for all three channels. For 6.25 μm channel, the error of RTTOV is smaller than those of FPM and ROM, while for 7.1 and 12 μm channel, the error of RTTOV is larger than those of FPM and ROM. Table 4 shows the RMSE of RTTOV, FPM, and ROM for all transmittance results. The RMSEs of FPM are almost the same as that of ROM for all channels. This is because ROM has a very small adjustment to the parameters of FPM. Therefore, despite the slight change in brightness temperature, the change in average transmittance is very small. In 6.25, 7.10, and 13.5 μm channels, the RMSE of RTTOV is smaller than that of FPM and ROM. In the other channels, the accuracy of FOM and ROM is higher. In Fig. 6, the maximum error of

Table 4. Transmittance RMSE Comparison of FPM, ROM, and RTTOV under 83 Standard Profiles

Channel	RTTOV	FPM	ROM
6.25 μm	0.0052	0.0140	0.0140
7.10 μm	0.0051	0.0070	0.0070
8.50 μm	0.0046	0.0042	0.0042
10.8 μm	0.0047	0.0018	0.0019
12.0 μm	0.0037	0.0009	0.0009
13.5 μm	0.0036	0.0079	0.0079

the RMSE of the 7.10 μm channel is larger than those of FPM and ROM. However, in Table 4, the overall error of FPM and ROM is larger than that of RTTOV. In other words, there is a systematic deviation in FPM and ROM in 7.10 μm channel.

Figure 7 shows the transmittance error contours for pressure from level to TOA calculated by RTTOV, FPM, and ROM under clear sky in 83 standard profiles. In general, the error comparison of the three schemes in the figure is basically the same as that in Table 4. The errors of the three schemes all increase as the altitude decreases. The RMSE of FPM and ROM in the upper atmosphere is slightly larger than that of RTTOV, while the error comparison in the lower atmosphere is consistent with the results in Table 4.

B. Real Profiles

We evaluated the accuracy of FPM for real atmospheric profiles. The data we used in the evaluation are as follows (Table 5).

The simulated time is 12:00 on August 19, 2019. We only consider the clear sky area for focusing only on the gaseous absorption. We show the observation of 6.25 and 10.8 μm channels in Fig. 8, and the errors of FPM and RTTOV are also shown. The gray part is the cloudy area. The accuracy of the three methods is almost the same in these two channels.

In 6.25 μm channel, the errors of three methods are generally negative, and the deviation of RTTOV is relatively larger; in 10.8 μm channel, the errors of three methods in the ocean area are close to 0, while the errors in the land area are all negative. This phenomenon of error distribution is probably caused by the fact that the value of the surface temperature data or the surface emissivity data is smaller than the actual value.

The errors of the three methods are all increased in real profiles. Therefore, we aim to analyze the sources of the error. We selected 1000 profiles randomly from the simulation area and calculated the reference results by LBL. Figure 9 shows the probability distribution of errors calculated by RTTOV, FPM, and ROM under all infrared channels. In 6.25 μm channel, the peak of FPM is at the same position as RTTOV, but its half-width is larger than RTTOV; the peak position of ROM is the closest to 0, and the half-width is the narrowest. In 13.5 μm channel, the peak positions of three methods are almost the same, but the half-widths of ROM and FPM are both larger than RTTOV. In the other channels, the accuracy of ROM and FPM is higher than that of RTTOV, and ROM has the highest accuracy. Table 6 illustrates the ME and RMSE of three methods compared with LBL under the 1000 profiles. The accuracy of FPM is better than RTTOV except 7.10 μm channel. In other words, the deviation between the profile data used in our calculation and the real profiles is the main limiting factor for FPM
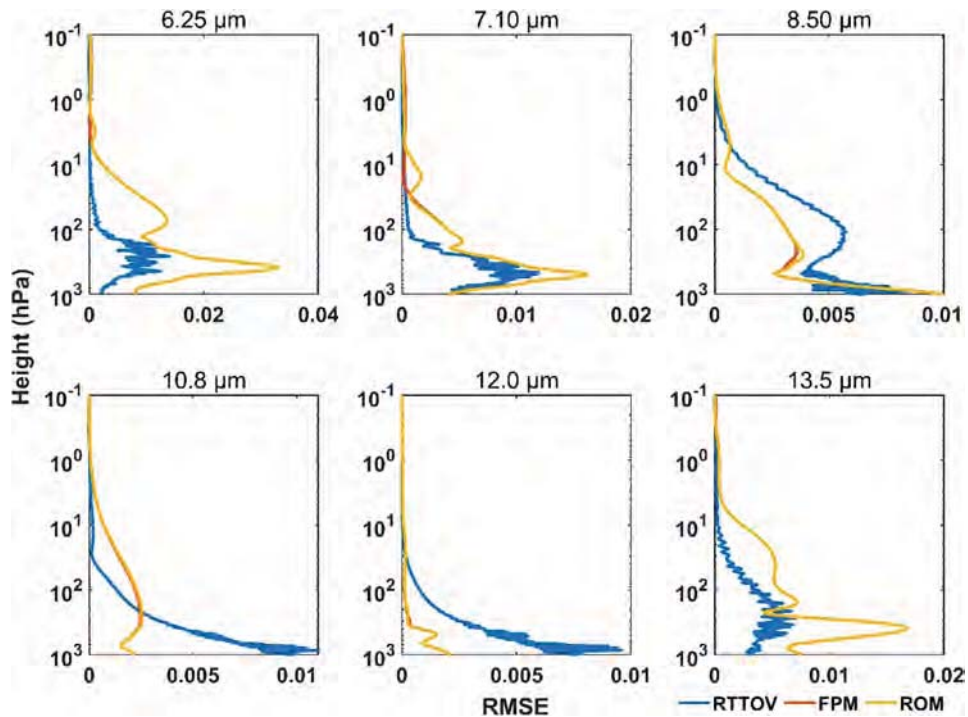
Fig. 7.   Transmittance error contours for pressure from level to TOA calculated by RTTOV, FPM, and ROM under clear sky in 83 standard profiles.

Table 5.   Input Data

Input Data	Source	URL
Atmospheric profiles	ERA-Interim	https://www.ecmwf.int/en/forecasts/dataset/ecmwf-reanalysis-interim
Land surface temperature		
Land surface emission		
Sea surface temperature data	NSMC	http://satellite.nsmc.org.cn/PortalSite/Data/Satellite.aspx
Cosine of viewing zenith angles		
Cloud detection data		

accuracy. Besides, we did not consider the effect of aerosol in our calculation. That can also be an error source.

Figure 10 shows the comparison of transmittance from level to TOA calculated by RTTOV, FPM, ROM, and LBL under clear sky in 1000 real profiles for 6.25, 10.8, and 13.5 µm channels. The errors of FPM are still almost the same as ROM. For 6.25 and 10.8 µm channels, the error of RTTOV increased, while the error of FPM and ROM decreased to be smaller than that of RTTOV. For 13.5 µm channel, RTTOV is slightly more accurate than FPM and ROM. Table 7 shows the RMSE of RTTOV, FPM, and ROM for all transmittance results. The RMSEs of FPM are still almost the same as ROM for all channels. For 6.25 and 7.10 µm channels, the RMSE of RTTOV is larger than that of FPM and ROM; for 8.50 µm channel, the RMSE of RTTOV is smaller than that of FPM and ROM. The results in these three channels are the opposite of the results under standard profiles. For 10.8 and 12.0 µm channels, the accuracy of FOM and ROM is still higher than RTTOV, while for 13.5 µm channel, the accuracy of FOM and ROM is still lower than that of RTTOV. In conclusion, the accuracy of FOM and ROM is still lower than that of RTTOV in 13.5 µm channel, but it is better than RTTOV in the other channels.

Figure 11 shows the transmittance error contours for pressure from level to TOA calculated by RTTOV, FPM, and ROM under clear sky in 1000 real profiles. The error comparison of the three schemes in the figure is basically the same as that in Table 4. Compared with the results of the standard profiles in Fig. 7, the error of FPM and ROM in the 8.50 µm channel becomes larger than RTTOV, while the large errors of other channels are less than or equal to RTTOV, and the transmittance error of FPM and ROM in the upper atmosphere is reduced to be consistent with RTTOV.

5. DISCUSSION

Compared with LBL, under the standard profiles, most brightness temperature results of FOM and ROM are better than RTTOV, but the transmittance accuracy of FPM and ROM in 6.25, 7.1, and 13.5 µm channels is lower than RTTOV. Under the real profiles, FPM and ROM not only have better brightness temperature results than RTTOV but also have better transmittance results for each channel. This is because the transmissivity of RTTOV is only from level to TOA, and its optimization process only focuses on the transmissivity from
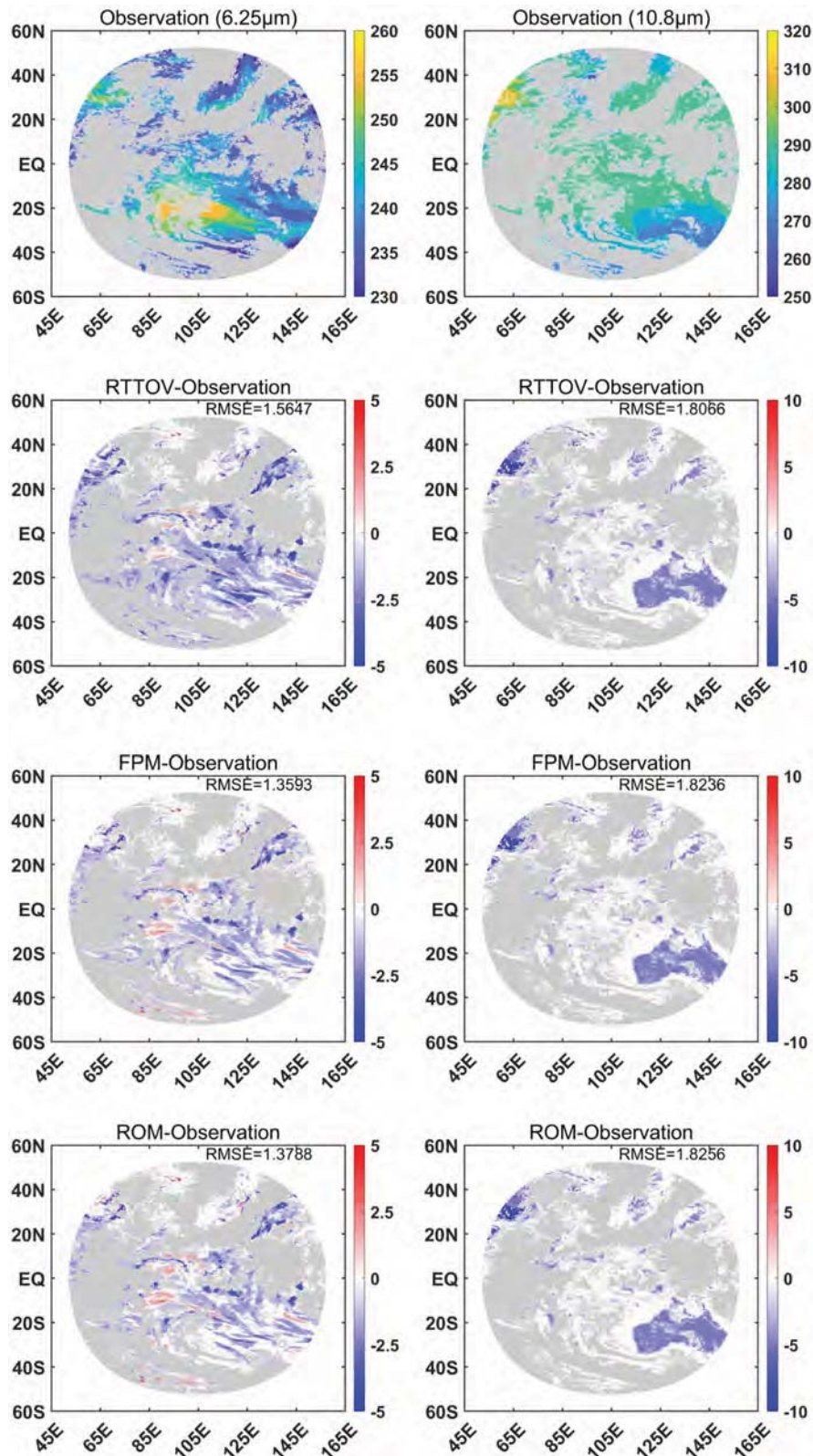
Fig. 8. Comparison between observations brightness temperature and simulated errors of RTTOV, FPM, and ROM under 6.25 μm and 10.8 μm channels. The gray area is cloud area. The unit is K.

level to TOA. In contrast, the results referred by FPM and ROM in the optimization process are heating rate and radiation flux,

that is, the transmittance from level to level that is weighted with temperature. Therefore, when FPM and ROM optimize
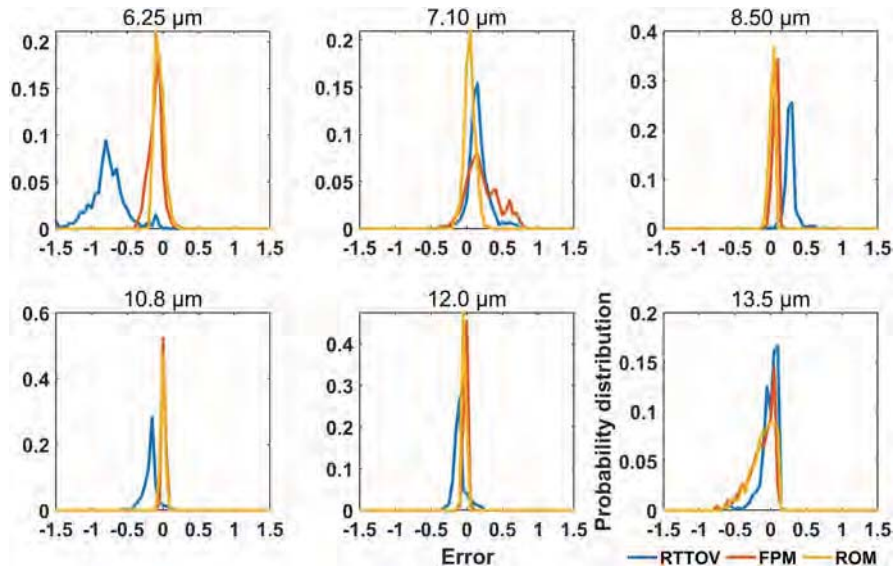
Fig. 9. Probability distribution of simulated brightness temperature errors calculated by RTTOV, FPM, and ROM under all infrared channels.

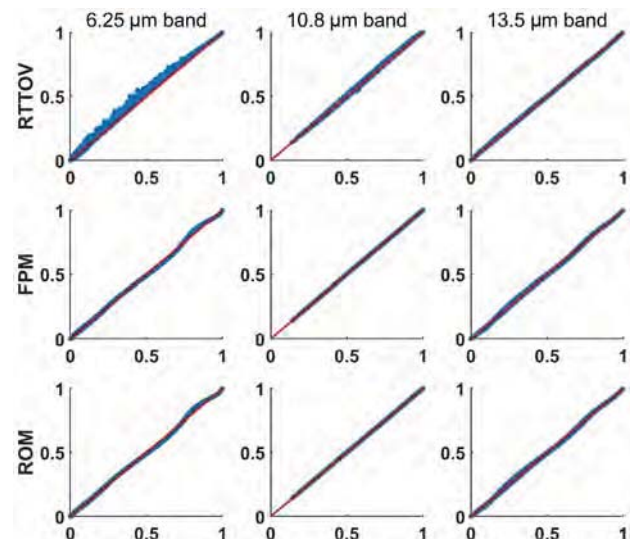**Table 6. Comparison of ME and RMSE of FPM, ROM, and RTTOV under 1000 Real Profiles**

Channel	ME[a] (K)			RMSE[b] (K)		
	RTTOV	FPM	ROM	RTTOV	FPM	ROM
6.25 μm	−0.77	−0.10	−0.05	0.8167	0.1383	0.0837
7.10 μm	0.16	0.22	0.04	0.2144	0.3128	0.0850
8.50 μm	0.28	0.07	0.02	0.2873	0.0752	0.0380
10.8 μm	−0.17	0.01	0.00	0.1951	0.0228	0.0227
12.0 μm	−0.10	−0.02	−0.04	0.1321	0.0283	0.0420
13.5 μm	0.02	−0.13	−0.11	0.1226	0.2184	0.2004

[a]ME, mean error.
[b]RMSE, root mean square error.

all transmissivity parameters to fit all results from level to level under standard atmosphere, the transmissivity results of level to TOA will inevitably become worse. On the other hand, because FPM and ROM focus on the results of all layers, they have better adaptability to the variation of level parameters—that is, under the actual atmospheric profile, the transmission accuracy of FPM and ROM is higher. Similarly, brightness temperature is actually the sum of atmospheric radiance from level to TOA converted into temperature. RTTOV only considered the result from level to TOA when optimizing parameters, but FPM and ROM considered different layer radiances. Therefore, the accuracy of FPM and ROM is better in practical application.

The main absorption gas properties are different in different channels, and the main source layers of radiance received by satellites and the sensitivity of the results to gas absorption parameters are different. For example, the radiation observed in 6.25 μm channel is mainly the radiation from the water vapor in the upper layer. In these layers, the water vapor content is small, but the absorption coefficient is large and varies dramatically, so the error generated in polynomial parameterization may cause large fluctuations in the results; the radiances observed in the 13.5 μm channel is mainly from the middle and bottom layer water vapor,where the water vapor content is high, but the


Fig. 10. Comparison of transmittance from level to TOA calculated by RTTOV, FPM, ROM, and LBL under clear sky in 1000 real profiles.

Table 7. Transmittance Comparison of ME and RMSE of FPM, ROM, and RTTOV under 1000 Real Profiles

Channel	RTTOV	FPM	ROM
6.25 μm	0.0125	0.0091	0.0091
7.10 μm	0.0055	0.0042	0.0042
8.50 μm	0.0024	0.0033	0.0033
10.8 μm	0.0065	0.0009	0.0009
12.0 μm	0.0044	0.0013	0.0013
13.5 μm	0.0044	0.0063	0.0063

absorption coefficient is relatively small, and polynomial parameterization can more easily simulate the change of the absorption coefficient. However, RTTOV only has the results from level to TOA, so we cannot compare the results from level to level.
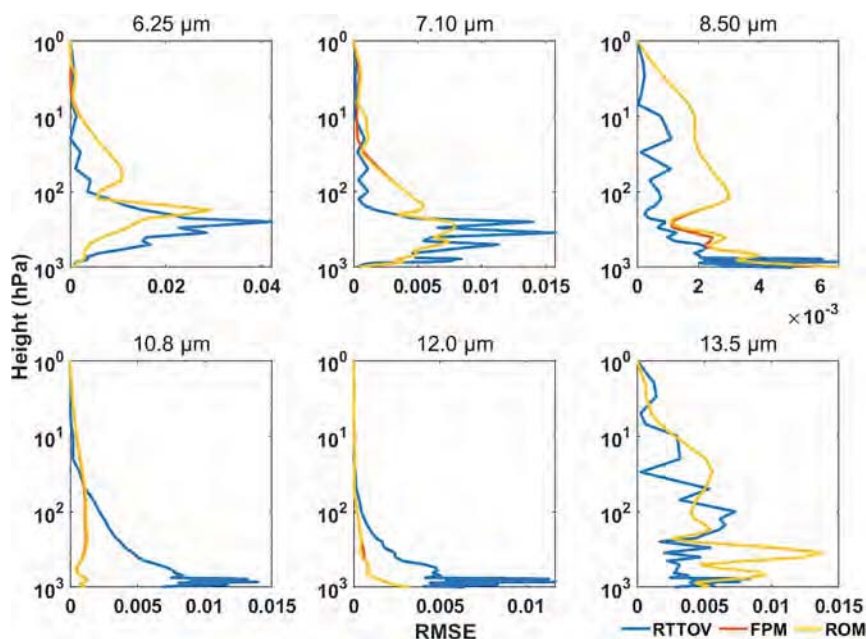
Fig. 11.   Transmittance error contours for pressure from level to TOA calculated by RTTOV, FPM, and ROM under clear sky in 1000 real profiles.

Focusing on this problem, we can adjust the optimization conditions of FPM to focus only on the results of level to ROA in the later works and make the top-level simulation more accurate.

6. CONCLUSION

In this paper, the FPM and ROM are modified and applied to the forward radiative transfer model for remote sensing of Fengyun 4A AGRI, and the simulated brightness temperature results are compared with LBLRTM and RTTOV. We modified the temperature interpolation formula of the gas absorption coefficient and the range of adjacent points in the iteration in FPM. Therefore, the constraints in ROM are greatly reduced. Besides, we have increased the number of standard atmospheric profiles in the optimal calculation.

Compared with the brightness temperature simulations of LBL, the accuracy of FPM and ROM are higher than that of RTTOV under both the standard atmospheric and the real profile, and ROM has the highest accuracy. Under the standard profiles, the minimum ME and RMSE of RTTOV are in 7.1 μm channel, with values of -0.0066 K and 0.1120 K, respectively. Both the two errors are lower than that of FPM, which are -0.032 K and 0.228 K, respectively, but still larger than that of ROM. The maximum ME of ROM is in 8.5 μm channel, with value of -0.0541 K. The error is larger than FPM, -0.0081 K, but still lower than RTTOV, 0.1968 K. Correspondingly, the RMSE of ROM shows the same comparison result in 8.5 μm channel, which is the error of ROM being larger than FPM but lower than RTTOV. In the other channels, the results show that ROM has the highest precision and RTTOV had the lowest precision. Under the real profiles, the errors of FPM in 7.1 μm and 13.5 μm channels are 0.22 K, -0.13 K for ME and 0.3128 K, 0.2184 K for RMSE, respectively, which are larger than that of RTTOV, with 0.16 K, 0.02 K, 0.2144 K, and 0.1226 K respectively. The ME and RMSE of ROM in 12.0 μm channel

are -0.04 K and 0.042 K, which are also larger than FPM with -0.02 K and 0.0283 K, and lower than RTTOV with -0.1 K and 0.1321 K. In the other channels, the results show that ROM has the highest accuracy and RTTOV has the lowest accuracy. Compared with satellite observations, the results of FPM, ROM, and RTTOV are not much different. There are two main factors that might cause this phenomenon: first, the input data interpolated from the coarse grid domain and the accuracy of the profiles can cause the bias of simulation; second, we did not consider the effects of aerosols in the simulated area.

For the channel average transmittance simulations, the accuracies of FPM and ROM are almost the same. For standard profiles, the errors of FPM and ROM are larger than RTTOV in 6.25, 7.1, and 13.5 μm channels, and the highest errors are in 6.25 μm channel, with the value of 0.014. In the other channels, FPM and ROM have better accuracy. For real profiles, the accuracy of FPM and ROM in 8.5 and 13.5 μm channels are slightly lower than RTTOV, but the differences did not reach 0.002, i.e., FPM and ROM perform better in real profiles. In 10.8 and 12.0 μm channels, the accuracies of FPM and ROM are always higher than RTTOV; in the other channels, the accuracy of FPM and ROM is better in real profiles but lower in standard profiles. In conclusion, FPM and ROM can achieve better results in the satellite remote sensing simulation.

REFERENCES

1. D. Efremenko, A. Doicu, D. Loyola, and T. Trautman, "Optical property dimensionality reduction techniques for accelerated radiative transfer performance: application to remote sensing total ozone retrievals," J. Quant. Spectrosc. Radiat. Transf. **133**, 128–135 (2014).

2. G. Hönninger, C. Friedeburgvon, and U. Platt, "Multi axis differential optical absorption spectroscopy (MAX-DOAS)," Atmos. Chem. Phys. **4**, 231–254 (2004).

3. K. L. Chan, A. Hartl, Y. F. Lam, P. H. Xie, W. Q. Liu, H. M. Cheung, J. Lampel, D. Pöhler, A. Li, J. Xu, H. J. Zhou, Z. Ning, and M. O. Wenig, "Observations of tropospheric NO_2 using ground based MAX-DOAS and OMI measurements during the Shanghai World Expo 2010," Atmos. Environ. **119**, 45–58 (2015).

4. K. L. Chan, M. Wiegner, M. Wenig, and D. Pöhler, "Observations of tropospheric aerosols and NO_2 in Hong Kong over 5 years using ground based MAX-DOAS," Sci. Total. Environ. **619**–620, 1545–1556 (2018).

5. D. P. Edwards and G. L. Francis, "Improvements to the correlated-*k* radiative transfer method: application to satellite infrared sounding," J. Geophys. Res. **105**, 18135–18156 (2000).

6. A. A. Lacis and V. Oinas, "A description of the correlated *k* distribution method for modeling nongray gaseous absorption, thermal emission, and multiple-scattering in vertically inhomogeneous atmospheres," J. Geophys. Res. **96**, 9027–9063 (1991).

7. R. M. Goody, R. West, L. Chen, and D. Crisp, "The correlated-k method for radiation calculations in nonhomogeneous atmospheres," J. Quant. Spectrosc. Radiat. Transf. **42**, 539–550 (1989).

8. Q. Fu and K. N. Liou, "On the correlated *k*-distribution method for radiative transfer in nonhomogeneous atmospheres," J. Atmos. Sci. **49**, 2139–2156 (1992).

9. G. Shi, "Effect of atmospheric overlapping bands and their treatment on the calculation of thermal radiation," Chin. Adv. Atmos. Sci. **1**, 246–255 (1984).

10. G. Shi, N. Xu, B. Wang, T. Dai, and J. Zhao, "An improved treatment of overlapping absorption bands based on the correlated *k* distribution model for thermal infrared radiative transfer calculations," J. Quant. Spectrosc. Radiat. Transf. **110**, 435–451 (2009).

11. C. Liu, Y. Ping, S. L. Nasiri, S. Platnick, K. G. Meyer, C. Wang, and S. Ding, "A fast visible infrared imaging radiometer suite simulator for cloudy atmospheres," J. Geophys. Res. **120**, 240–255 (2015).

12. S. Yang, P. Ricchiazzi, and C. Cautier, "Modified correlated *k*-distribution method for remote sensing," J. Quant. Spectrosc. Radiat. Transf. **64**, 585–608 (2000).

13. M. D. Chou, M. J. Suarez, X. Z. Liang, and M. H. Yan, "A thermal infrared radiation parameterization for atmospheric studies," NASA Technical Memo. 104609 (2001), p. 56.

14. F. Liu and G. J. Smallwood, "An efficient approach for the implementation of the SNB based correlated-*k* method and its evaluation," J. Quant. Spectrosc. Radiat. Transf. **84**, 75–465 (2004).

15. M. F. Modest and R. J. Riazzi, "Assembly of full-spectrum k-distributions from a narrow-band database, effects of mixing gases, gases and nongray absorbing particles, and mixtures with nongray scatters in nongray enclosure," J. Quant. Spectrosc. Radiat. Transf. **90**, 89–169 (2005).

16. J. Li and H. W. Barker, "A radiation algorithm with correlated-*k* distribution. Part I: Local thermal equilibrium," J. Atmos. Sci. **62**, 286–309 (2005).

17. F. Zhang, M. Zhu, J. Li, W. Li, D. Di, Y.-N. Shi, and K. Wu, "Alternate mapping correlated k-distribution method for infrared radiative transfer forward simulation," Remote Sens. **11**, 994 (2019).

18. M. Zhu, S. Jin, J. Tao, and X. Wu, "Automatic methods for gas absorption calculation based on correlated k-distribution," J. Quant. Spectrosc. Radiat. Transf. **270**, 107697 (2021).

19. T. Nakajima, M. Tsukamoto, Y. Tsushima, A. Numaguti, and T. Kimura, "Modeling of the radiative process in an atmospheric general circulation model," Appl. Opt. **39**, 4869–4878 (2000).

20. X. Otazu, M. Gonzalez-Audicana, O. Fors, and J. Nunez, "Introduction of sensor spectral response into image fusion methods. Application to wavelet-based methods," IEEE Trans. Geosci. Remote Sens. **43**, 2376–2385 (2005).

21. A. Berk, "Analytically derived conversion of spectral band radiance to brightness temperature," J. Quant. Spectrosc. Radiat. Transf. **109**, 1266–1276 (2008).

22. Y. Chen, F. Weng, H. Yong, and Q. Liu, "Planck-weighted transmittance and correction of solar reflection for broadband infrared satellite channels," J. Atmos. Ocean. Technol. **29**, 382–396 (2011).